International Journal of Earth Sciences (2021) 110:791–808
https://doi.org/10.1007/s00531-021-01990-5

ORIGINAL PAPER

The youngest matrix of 234 Ma of the Kanguer accretionary mélange containing blocks of N-MORB basalts: constraints on the northward subduction of the Paleo-Asian Kanguer Ocean in the Eastern Tianshan of the Southern Altaids

Songjian Ao[1,2,3] · Qigui Mao[4,5] · Brian F. Windley[6] · Dongfang Song[1,2,3] · Zhiyong Zhang[1,2,3] · Ji'en Zhang[1,2,3] · Bo Wan[1,2,3] · Chunming Han[1,2,3] · Wenjiao Xiao[1,2,3,4]

Received: 18 September 2020 / Accepted: 15 January 2021 / Published online: 7 February 2021

Abstract
The Altaids accreted around, and grew southward, from the Siberian craton, but the time of final amalgamation of this orogen is still controversial. The Eastern Tianshan in the southernmost Altaids is characterized by multiple, late, accreted arcs and thus is an ideal tectonic environment to answer the time of final amalgamation of the Altaids. In this study we report the results of new field-based lithological mapping and structural analysis on the Kanguer mélange in the Eastern Tianshan, which is composed of blocks of basalt, chert, limestone, and other rocks within a strongly deformed and cleaved matrix of sandstone and schist. Our geochemical and isotopic data of basaltic blocks from several parts of the Kanguer mélange show they are relics of Normal-Mid-Ocean-Ridge (N-MORB)-type oceanic lithosphere, and U–Pb ages and Hf isotopes of detrital zircons from the matrix sandstones indicate they were derived only from the Dananhu arc to the north. Accordingly, our interpretation is that the Kanguer mélange was part of an accretionary complex that fringed the Dananhu arc, and therefore the subduction polarity of the Kanguer Ocean was to the north (present coordinates). The maximum depositional ages (MDAs) of our three sandstone samples (08K01, 08K02, and 08K03) from the mélange matrix were 234 ± 14 Ma, 242.5 ± 1.3 Ma, and 236 ± 2.0 Ma respectively, indicating that the Kanguer Ocean was still being subducted at ca. 234 Ma, and the accretion of the Kanguer mélange must have lasted until that time, when the accretionary complex was still located opposite to the Yamansu-CTS accretionary complex to the south. Thus, the final amalgamation of the Dananhu and Yanmansu-CTS arcs took place by the welding of two accretionary complexes in the late Middle Triassic (Ladinian) in this part of the southern Altaids. Integration with relevant amalgamation histories throughout the Tianshan indicates that the time of terminal amalgamation in the southern Altaids was probably in the Middle-Late Triassic, which is much younger than previously envisaged.

Keywords Detrital zircon · U–pb ages · Accretionary mélange · Final amalgamation time · Altaids

✉ Songjian Ao
asj@mail.iggcas.ac.cn

✉ Qigui Mao
qg_mao@sina.cn

✉ Wenjiao Xiao
wj-xiao@mail.iggcas.ac.cn

[1] State Key Laboratory of Lithospheric Evolution, Institute of Geology and Geophysics, Chinese Academy of Sciences, Beijing 100029, China

[2] Innovation Academy for Earth Science, CAS, Beijing, China

[3] College of Earth and Planetary Sciences, University of Chinese Academy of Sciences, Beijing 100049, China

[4] Xinjiang Research Center for Mineral Resources, Xinjiang Institute of Ecology and Geography, Chinese Academy of Sciences, Beijing, China

[5] Beijing Institute of Geology for Mineral Resources, Beijing 100012, China

[6] Department of Geology, The University of Leicester, Leicester LEI 7RH, UK

Introduction

The Altaids or the southern Central Asian Orogenic Belt, one of the largest accretionary orogens in the world (Fig. 1a), accreted around, and grew southward from, the Siberian craton by the successive accretion of many arcs, accretionary complexes and micro-continents (Bazhenov et al. 2003; Buchan et al. 2002; Coleman 1989; Dobretsov et al. 1995; Şengör and Natal'in 1996; Şengör et al. 1993; Wilhem et al. 2012; Windley et al. 2007; Xiao et al. 2013, 2018), but there are several contrasting and controversial tectonic models to explain that growth (Bazhenov et al. 2003; Şengör and Natal'in 1996; Windley et al. 2007; Xiao et al. 2013, 2015). Also controversial is the time of final accretion and amalgamation, which varies from the Carboniferous (Gao and Klemd 2003; Han and Zhao 2018; Qin et al. 2011; Zhou et al. 2004) to the Permo-Triassic (Huang et al. 2018; Mao et al. 2014b; Windley et al. 2007; Xiao et al. 2010; Xiao et al. 2004). Accordingly, the Eastern Tianshan, being located in the southernmost Altaids, provides critical information about the final time of amalgamation.

The Eastern Tianshan is the graveyard of many island arcs and accretionary wedges (Windley et al. 1990; Xiao et al. 2010, 2004). The youngest age of the matrix of an accretionary wedge is close to the final amalgamation time, a detrital zircon U–Pb age is a useful constraint on sediment provenance (Benyon et al. 2014; Fedo et al. 2003; Matthews et al. 2017; Sharman et al. 2015), the youngest detrital zircon can constrain the MDA (Coutts et al. 2019; Fedo et al. 2003; Nelson 2001), and the lag time between zircon crystallization and deposition is commonly very short (Cawood et al. 2012). Therefore, the MDA of detrital zircons is a useful method to constrain the time of deposition of sediments in arc-adjacent basins and accretionary complexes, particularly where biostratigraphic and magnetostratigraphic ages are unavailable (Coutts et al. 2019; Sickmann et al. 2018).

The aim of this publication is to report the results of new field-based lithological mapping and structural analysis of the Kanguer mélange in the Eastern Tianshan, which has a block-in-matrix structure. We present new isotopic data of the Maximum Deposition Age (MDA) of the sandstone matrix, and new geochemical data of basaltic blocks in the mélange. The MDA of three samples is consistent, ranging from 234 ± 14 Ma to 242.5 ± 1.3 Ma, and the basalts have an N-MORB chemical affinity. With these data we demonstrate that the Kangure Ocean, a branch of the Paleo-Asian Ocean, had a far younger subduction record than previously envisaged. Therefore, the time of final amalgamation of the Altaids in the Tianshan was most likely in the late Middle Triassic (Ladinian).

Geological background

The Eastern Tianshan, situated between the Siberian craton to the north and the Tarim craton to the south, occupies the bulk of the southmost Altaids (Fig. 1a), and comprises

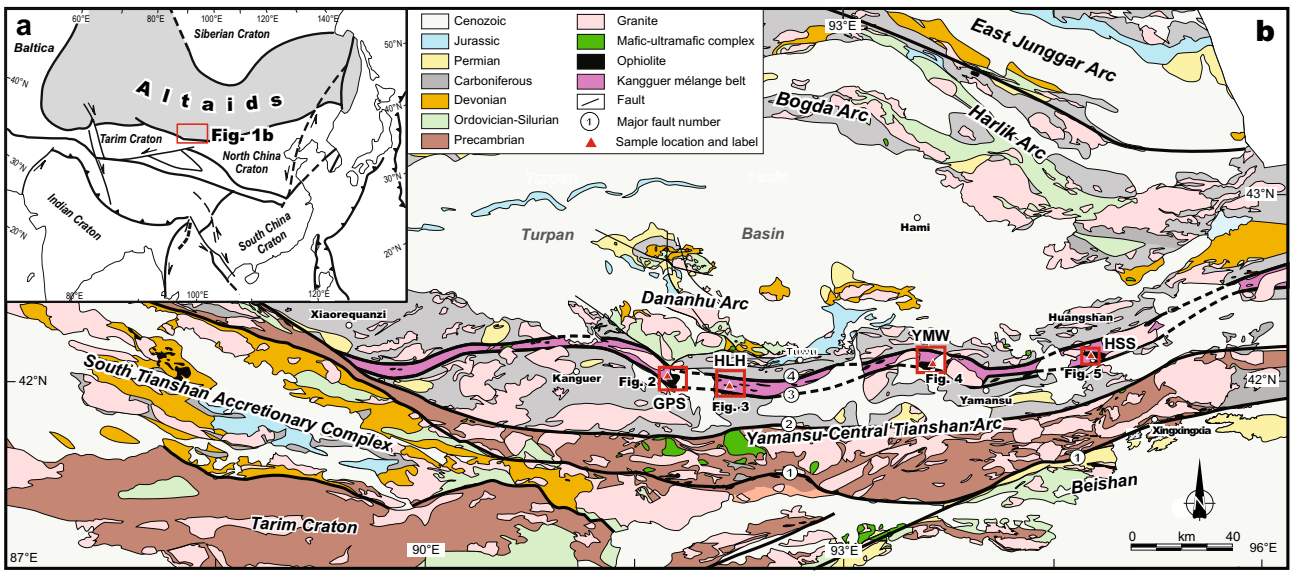

Fig. 1 **a** Schematic tectonic map of Central Asia (Şengör et al. 1993; Xiao et al. 2018) showing the position of the Eastern Tianshan in **b**. **b** The geological map of the Eastern Tianshan showing the distribution of the main tectonic unit (modified after Xiao et al. 2004). The locations of the samples and of Fig. 2 are marked. ① Kawabulake-Xingxingxia fault, ② Aqikekuduke-Shaquanzi fault, ③ Yamansu-Kushui fault, ④ Kanguer fault

E/W-trending accretionary belts, which include continental margin arcs, microcontinents, island arcs, ophiolites, and accretionary wedges (Qin et al. 2011; Xiao et al. 2004, 2018). The internal tectonic units of the orogen are from north to south (Fig. 1b): the Dannanhu arc, the Kanguer mélange, the Yamansu arc, the Central Tianshan block, and the Southern Tianshan accretionary complex.

The Dannanhu arc is composed predominantly of Ordovician to Permian tholeiitic basalts, calc-alkaline andesites, pyroclastic rocks, and tuffs (Du et al. 2018a, b, 2019; Qin et al. 2011; Wang et al. 2018). The Yamansu arc consists of Devonian-Carboniferous volcanic and intrusive rocks (Du et al. 2019; Luo et al. 2016), which (Chen et al. 2019) interpreted as a continental arc built on the margin of the Central Tianshan Arc. The Central Tianshan block comprises calc-alkaline basaltic andesites, volcaniclastic rocks, minor I-type granites, and a Precambrian basement (Long et al. 2020; Ma et al. 2014; Mao et al. 2018) and the South Tianshan accretionary complex contains discontinuous slices of Mid-Devonian to Early Carboniferous ophiolites (Ao et al. 2020; Gao and Klemd 2003; Sang et al. 2020).

The Kanguer mélange is situated between the Kanguer fault in the north and the Yamansu-Kushui fault in the south (Fig. 1c); it was previously mapped as the Carboniferous Wutongwozi Formation (XBGMR 1993). It is thrust-imbricated and dismembered, and thus contains blocks of serpentinite, gabbro, basalt, limestone, and chert in a metasandstone matrix. The Kanguer mélange has been variously interpreted as an inter-arc basin between the Dannanhu and Yamansu arcs (Han and Zhao 2018; Xiao et al. 2004), as a component in the final suture zone that separates the Siberian craton to the north and the Tarim craton to the south (Ma et al. 1997), and as an accretionary wedge in a short-lived minor ocean that formed in the Carboniferous (Wang et al. 2019).

Field observations and sampling

In order to understand the composition and structure of the Kanguer mélange, four areas from west to east were mapped in detail: the Gas pipeline station (GPS), the Haluo highway (HLH), the Yamansu West (YMW), and the Huangshan South (HSS) (Figs. 1, 2). Our resultant maps included previous map data (XBGMR 1993). We describe below the main lithologies and structures that are representative of the whole Kanguer mélange.

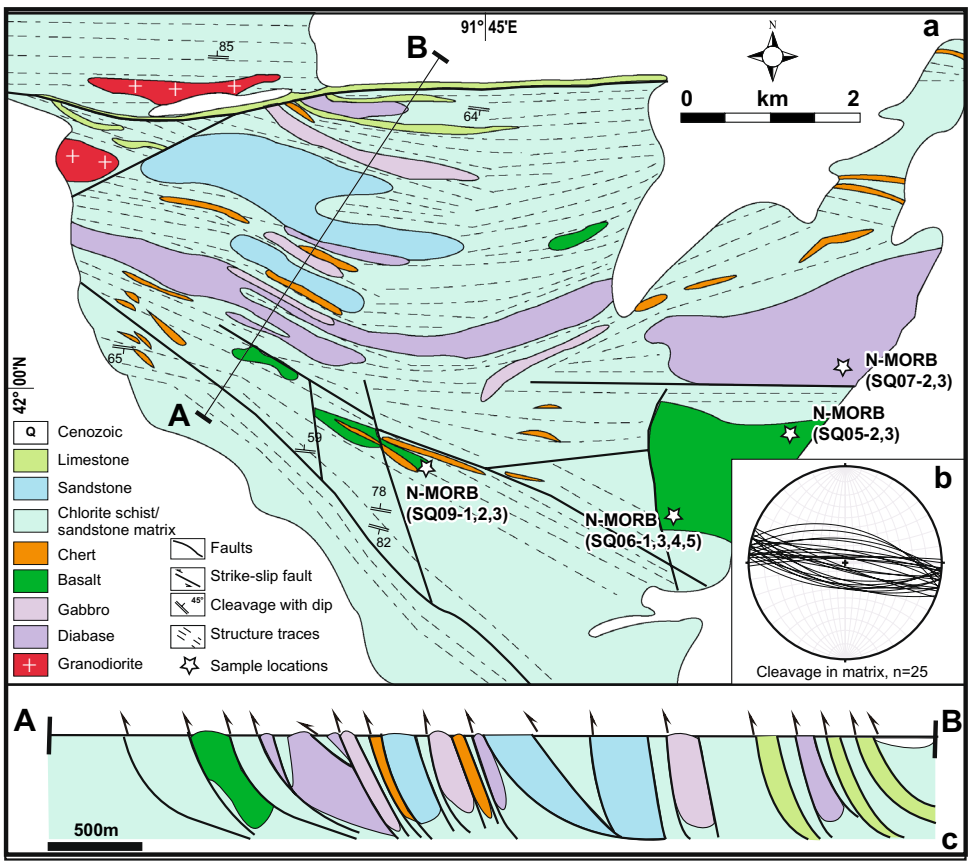

Fig. 2 **a** A geological map of the GPS area in the Kanguer mélange showing the block-in-matrix structure. Sample locations and cross-section are marked. **b** Stereographic projection of cleavages from the matrix. All stereonet plots are equal-angle lower-hemisphere projections, utilizing Stereonet 11 of (Cardozo and Allmendinger 2013). **c** The cross-section illustrates the thrust-imbrication of blocks in the matrix of sandstone and chlorite schist

The GPS area

The Kanguer mélange has a characteristic block-in-matrix structure (Fig. 2a). The matrix is mainly composed of chlorite-phyllite schist and meta-sandstone, which have a strong slaty cleavage that strikes almost E-W and dips moderately to sub-vertical (Fig. 2b). The primary depositional features of the matrix sediment are difficult to discern, because they have been heavily overprinted by the strong cleavage. The blocks consist of limestone, chert, sandstone, basalt, diabase, and gabbro that have been thrust-imbricated (Fig. 2c). Granodiorite intrusions crop out as elongate E/W-trending blocks (see upper left corner of Fig. 2a). The limestone and diabase blocks generally form ribbons that are several kilometers long. The cherts mostly occur in lenses that are several meters to several hundred meters long that have aspect ratios of 1:3 to 1:10, and their long axes are parallel to enclosing cleavage and to other lithologies. The gabbros and basalts form elongate blocks whose long axes are aligned sub-parallel to the main EW-trending faults. We consider the blocks of basalt, diabase, gabbro, limestone, and chert to be fragments of ocean plate stratigraphy, which were mixed and accreted in the original accretionary wedge. Samples from eleven basaltic blocks (SQ05-2/3, SQ06-1/3/4/5, SQ07-2/3, and SQ09-1/2/3) were collected (Fig. 2a) and analyzed to constrain their tectonic setting.

The HLH area

In the HLH area the Kanguer mélange has a block-in-matrix structure in which blocks of gabbro, massive basalt, pillow basalts, diabase dykes, chert, limestone, and sandstone/siltstone are embedded and imbricated in a matrix of chlorite-phyllite schist and cleaved sandstone (Fig. 3a). The matrix sandstones and chlorite-phyllites are highly cleaved and were intruded by large quartz veins indicating the movement of hydrothermal fluids during the shearing (Fig. 3a). The EW-trending, subvertical cleavage in the matrix in the northern (Fig. 3b) and central (Fig. 3c) parts of the HLH area is penetrative and has overprinted the bedding so strongly that the primary depositional structures are mostly difficult to observe.

In the central-northern parts of the HLH area, the blocks of gabbro, diabase, and basalt crop out in discontinuous lenses or ribbons ranging in length from several meters to several hundred meters. The blocks of gabbro and basalt are elongate with their long axes aligned sub-parallel to the main bounding faults of the mélange. The cherts generally crop out as lenses ranging in length from several meters to a kilometer with aspect ratios from 1:1.5 to 1:7 with their long axes parallel to the adjacent cleavage. The contacts between the blocks and matrix are thrusts. The blown sandstones, red cherts, and massive green basalts have a clear imbricate structure indicating they have been thrust to the south (Fig. 6a, b). Both the basalt and chert blocks are more strongly cleaved close to their bordering thrust planes (Fig. 7a, b).

Sandstone blocks in the south of the HLH area are huge—several kilometers wide and tens of kilometers long. The limestone blocks form ribbons or discontinuous lenses ranging in length from several meters to tens of kilometers. The sandstones and limestones retain their primary sedimentary bedding, and appear to be locally coherent in the Kanguer mélange. The thick sandstone blocks are intruded by elongate granodiorite dykes that are folded but only weakly cleaved; the long axes of the granodiorite intrusions are parallel to the regional cleavage. Folded bedding planes indicate tight to isoclinal sub-vertical folds in sandstone (Fig. 3d), the axes of which are parallel to the east–west cleavage of the matrix. Overall, these structures indicate a regional N–S compression.

The thrusts and cleavages in the entire HLH area of the Kanguer mélange are displaced by late NW/SE-trending dextral strike-slip faults. The blocks of sandstone and basalt are thrust slices, which belong to top-to-the-south thrust duplexes (Figs. 6, 7). All these structures indicate that the blocks of basalt, diabase, gabbro, limestone, sandstones and chert probably formed in different environments, and were inter-mixed during addition to the accretionary complex. Three sandstone samples (08K01, 02, and 03) were collected in the HLH area and their detrital zircons were analyzed for U–Pb dating, Hf isotopes and whole-rock major and trace elements. Thirteen basalt samples (HL01-1/3/4, HL05-1/2, and HL07-14) were collected (Fig. 3a) for whole-rock geochemical analyses to constraint their tectonic setting.

The YMW area

In the YMW area the Kanguer mélange has a block-in-matrix structure and has been intruded by granodiorite plutons (Fig. 4). The sandstone/pelite matrix has an E-W cleavage that is so pervasive that primary depositional structures are rarely preserved. The blocks are mainly basalts that range from hundreds of meters to several kilometers in size, and a few ribbon lenses of limestone and chert. In the north of the YMW area the basaltic blocks are elongate with their long axes aligned sub-parallel to the main thrust faults, but in the south the basalt blocks are juxtaposed and separated only by thrusts that are marked by ribbons of foliated limestone and chert. The southern part of the YMW area possibly contains dismembered remnants of oceanic plate stratigraphy, and the whole YMW area likely came from a high-strain section of an accretionary complex. Eighteen basalts were sampled (YM16-1/2/4/5/6, YM17, et al.) for geochemical analysis to constrain the tectonic setting of the Kanguer mélange.

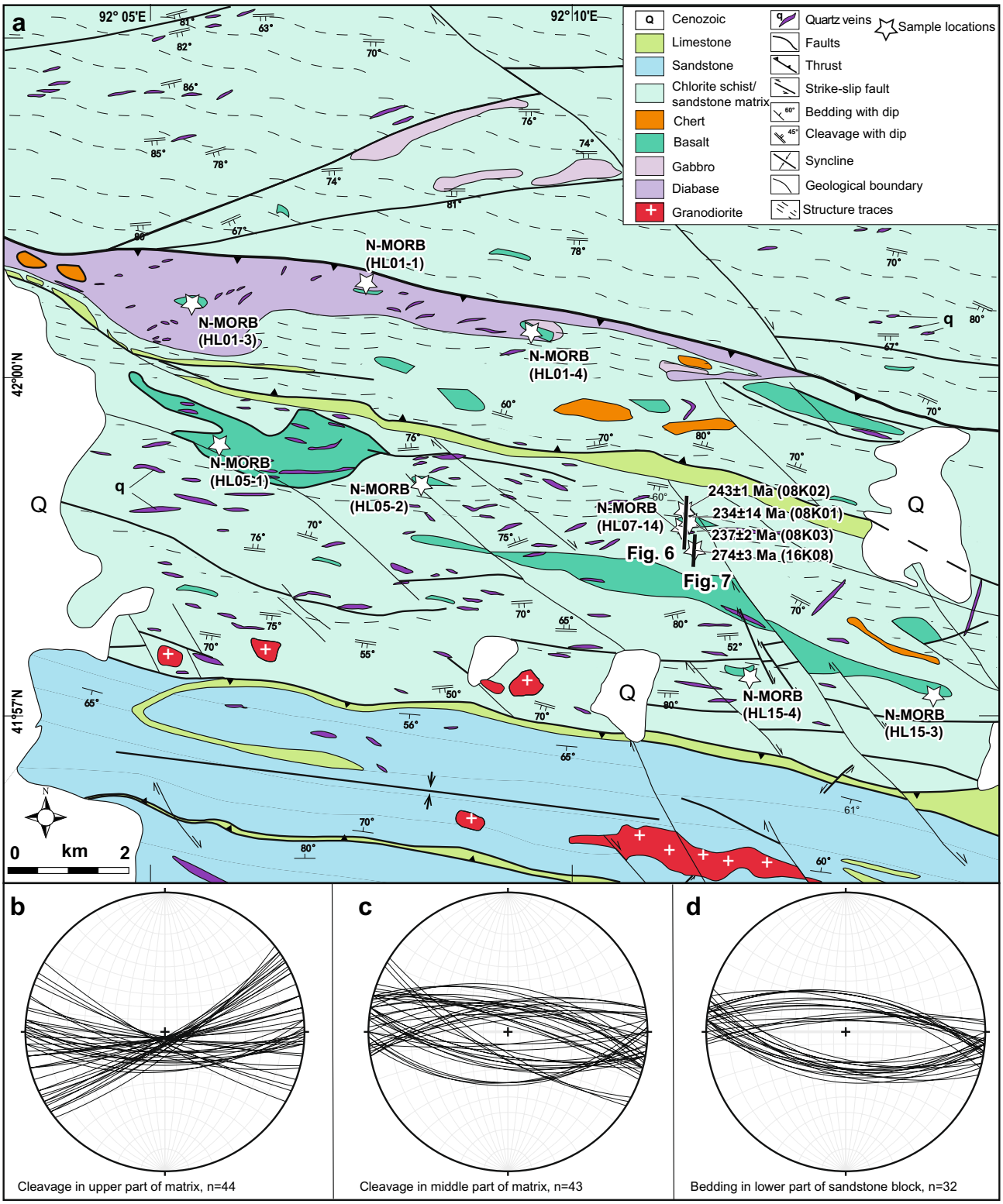

Fig. 3 **a** A geological map of the HLH area in the Kanguer mélange showing the block-in-matrix structure. The locations of Figs. 6 and 7 are marked. **b**, **c** Stereographic projections of cleavages in the mélange matrix in the northern and middle areas. **d** Stereographic projection of bedding planes in a sandstone block in the southern part of **a**

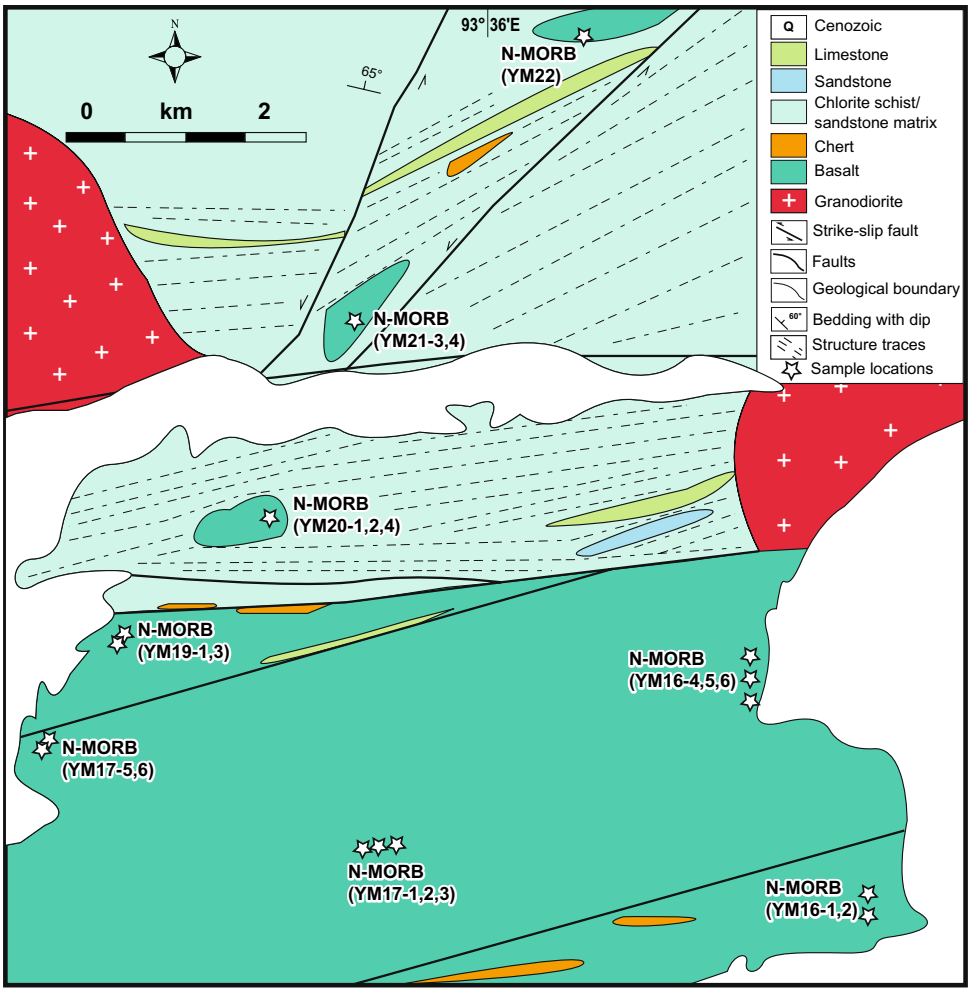

Fig. 4 A geological map of the YMW area in the Kanguer mélange showing two discordant granodiorite intrusions, and the sample locations

The HSS area

In the southern HSS area the Kanguer mélange also has a block-in-matrix structure (Fig. 5a). The blocks are mainly of basalt, limestones, chert, and sandstone. The blocks of limestone and basalt are elongated with their long axes sub-parallel to the main enclosing faults. The cherts generally outcrop as lenses that range in length from several meters to a kilometer, and their aspect ratios range from 1:5 to 1:11. The contacts between the blocks and matrix are thrusts. The margins of the blocks are typically fractured and foliated; the foliation is parallel to the long axes of the blocks and to the cleavage of the matrix. The matrix consists of chloritic to phyllitic meta-siltstone/sandstone, which is cleaved and locally folded (Fig. 5b, c). The bedding planes outline tight to isoclinal sub-vertical folds (Fig. 5b), the axes of which are parallel to the E/W-trending cleavage of the matrix. In the northern part of the area the chloritic-phyllitic siltstones/sandstones and the basalts belong to thrust imbricates, which indicate top-to-south compression. The whole Kanguer mélange in the HSS area is transected by several NE/SW-trending dextral strike-slip faults. Five basalts (HS19-2/3/4/6/7) were sampled from the area for geochemical analysis.

Geochemical results

Whole-rock analysis

Whole-rock major and trace elements of the basalts are listed in Appendix Table 1.

The major element compositions of eleven whole-rock tholeiitic basalts (Fig. 10b) from the GPS area vary across a relatively narrow range with $SiO_2 = 46.0–48.5$ wt%, $Al_2O_3 = 14.2–15.3$ wt%, $CaO = 8.8–10.9$ wt%, and $MgO = 6.8–7.9$ wt%. These basalts exhibit relatively high Cr (81–252 ppm) and Ni (62–103 ppm) concentrations. The Na_2O concentrations are somewhat variable, possibly reflecting seawater alteration. Rare earth element (REE) patterns of the basalts (Fig. 9a) are comparable to those of N-MORBs with $(La/Yb)_N$ contents ranging from 1.7 to 2.0,

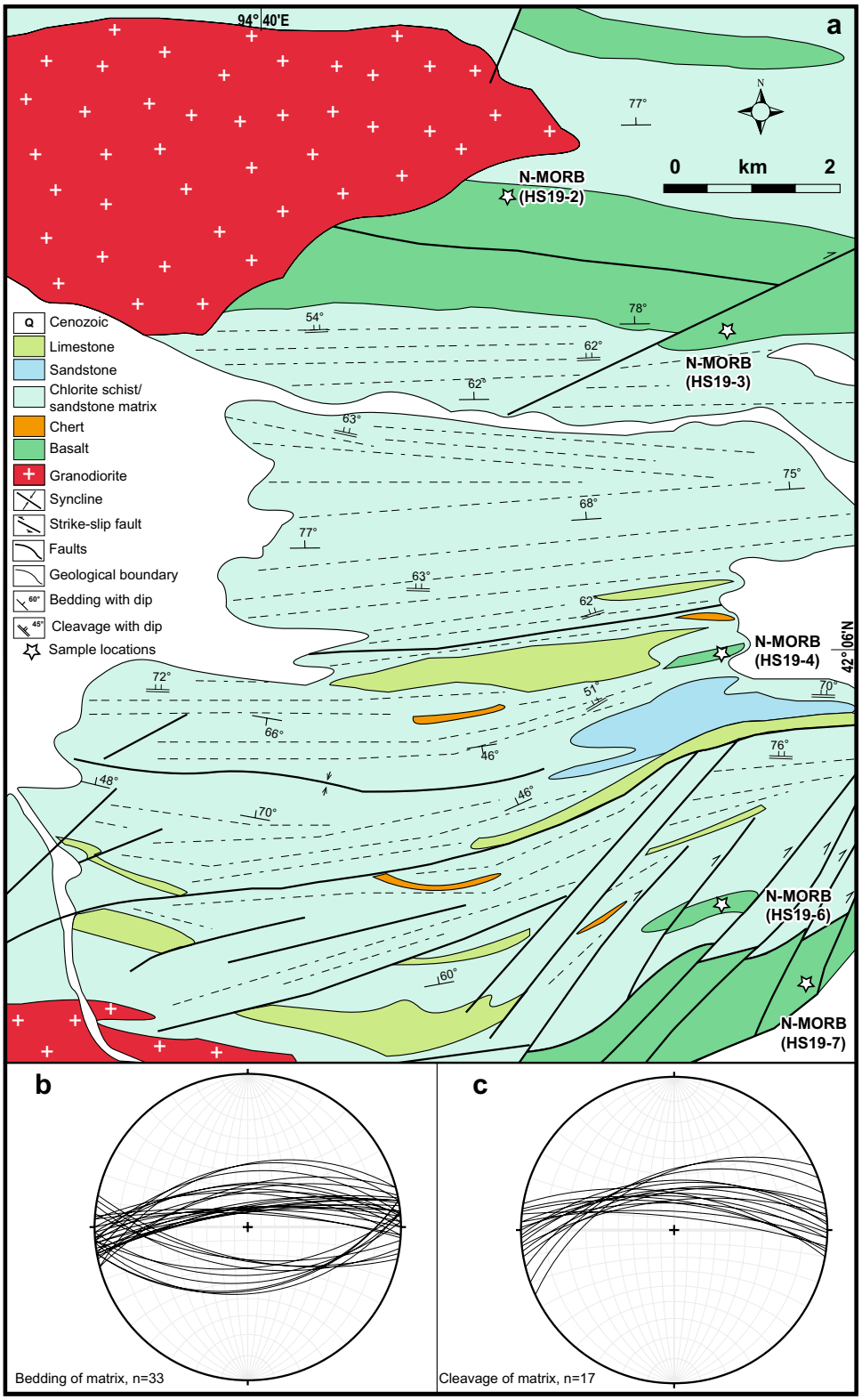

Fig. 5 **a** A geological map of the HSS area in the Kanguer mélange showing lens-shaped blocks in the matrix, a discordant granodiorite intrusion and the sample locations. **b**, **c** Stereographic projections of the planes of bedding and cleavage of the matrix

and with positive Ba and Sr anomalies and a negative Gd anomaly (Fig. 9b).

Thirteen basalt samples from the HLH area have relatively narrow elemental ratios with SiO_2 = 43.7–48.6 wt%, Al_2O_3 = 13.1–16.4 wt%, CaO = 7.3 –11.6 wt%, and MgO = 6.3–8.4 wt%. These basalts exhibit relatively high Cr (184–228 ppm) and Ni (76–111 ppm) concentrations. The samples are altered and thus have variable contents of

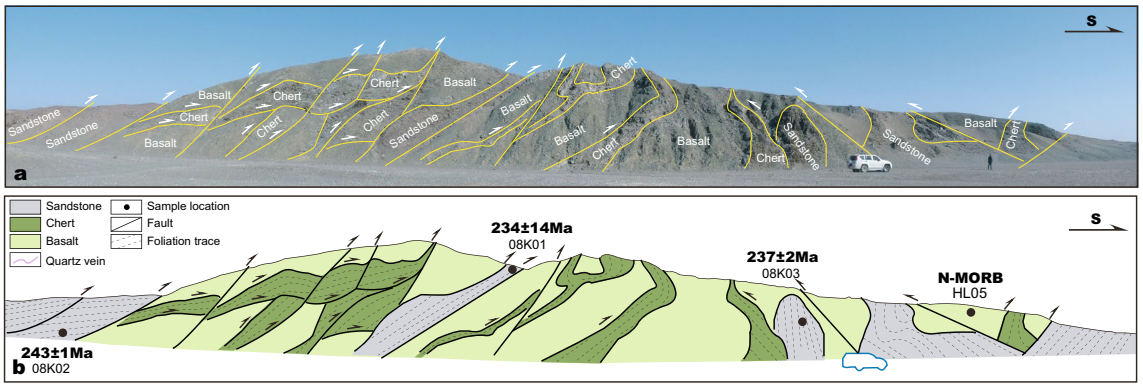

Fig. 6 **a** Field photo of a long cliff face that gives a structural cross-section showing multiple thrusts and imbrication of chert and basalt layers in the Kanguer mélange. **b** An illustrative sketch of the cliff section shown in (**a**). Sample locations and labels are marked. Jeep for scale

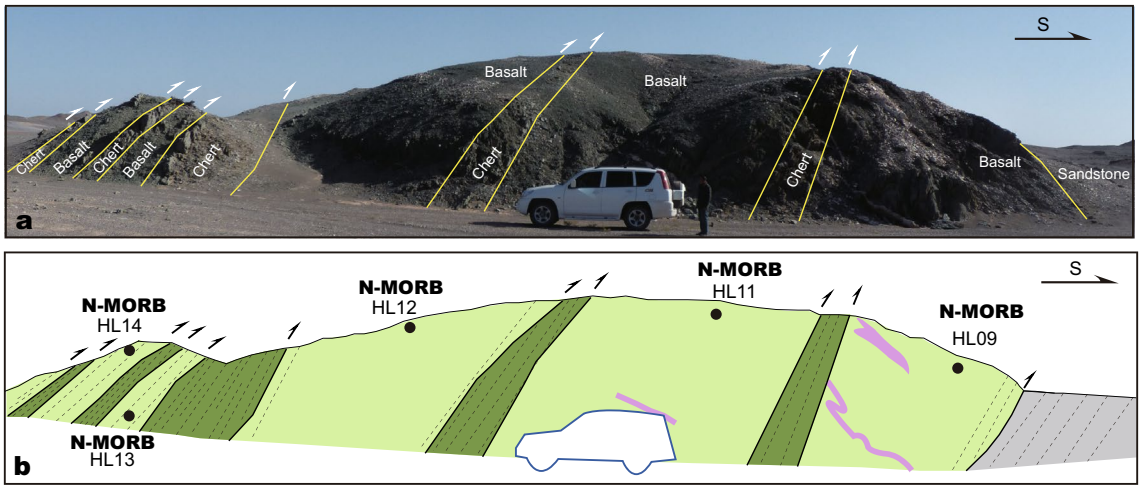

Fig. 7 **a** Cross-section showing the typical imbricate structure of thrusted layers and lenses of chert and basalt of the Kanguer mélange. **b** A sketch cross-section explaining the details in **a**. Sample locations and labels are marked. The legends are same to those of Fig. 6. Jeep for scale

LOI ranging from 2.2 to 40.5 wt%. Na_2O concentrations in the whole rocks are variable from 1.42 to 4.01 wt%, likely reflecting seawater alteration. REE patterns (Fig. 9c) are similar to those of N-MORBs with $(La/Yb)_N$ ratios between 0.8 and 2.0; some basalts have positive Ba, Sr, and Zr anomalies and a slightly negative Gd anomaly (Fig. 9d).

Eighteen basalts from the YMW area have contents of $SiO_2 = 41.9–46.7$ wt%, $Al_2O_3 = 10.7–17.8$ wt%, $CaO = 8.5–14.3$ wt%, and $MgO = 3.6–11.9$ wt%. These basalts exhibit relatively high Cr (293–817 ppm) and Ni (115–894 ppm) concentrations. Na_2O concentrations in whole rocks are variable from 0.9 to 4.2 wt%, maybe reflecting seafloor alteration. REE patterns (Fig. 9e) are comparable to those of N-MORBs with $(La/Yb)_N$ ratios between 0.5 and 1.7, and they have positive Ba and Sr anomalies and negative Gd and Ti anomalies (Fig. 9f).

The major element compositions of five basalts from the HLH area have variable contents of $SiO_2 = 42.1–52.9$ wt% and $CaO = 5.8–9.1$ wt%, and relatively narrow ranges of $Al_2O_3 = 12.2–14.1$ wt%, and $MgO = 2.3–3.8$ wt%. These basalts exhibit slightly low Cr (33–40 ppm) and Ni (34–51 ppm) concentrations. REE patterns (Fig. 9g) are like those of N-MORBs, with $(La/Yb)_N$ ratios of 0.6–0.7, and they have a positive Ba anomaly and negative Sr and Ti anomalies (Fig. 9h).

Sr–Nd isotopes

Ten whole-rock basalts were analyzed for their Sr and Nd isotopes; the results are listed in Appendix Table 2 and shown in Fig. 12b. Two basalts from the GPS area have high initial $(^{87}Sr/^{86}Sr)_i$ ratios of 0.706040 and 0.706876, and $\varepsilon_{Nd}(t)$ values of +8.30 and +9.34. Five basalts from the HLH area have an initial $(^{87}Sr/^{86}Sr)_i$ ratio that varies from 0.701248 to 0.707631, and $\varepsilon_{Nd}(t)$ values of +8.33 and +9.45. Three basalts from the YMW area have an initial

Fig. 8 Micro-photos of dated samples. **a** Sample 08K01, showing poor sorting, high proportions of detrital altered matrix. Grains are angular and subrounded. **b** Sample 08K02 and **c** Sample 08K03, showing weak-orientated and poor sorting, high proportions of detrital and diagenetically altered matrix and a mix of quartz, feldspar and lithic framework fine grains

$(^{87}Sr/^{86}Sr)_i$ ratio that ranges from 0.703681 to 0.705359, and $_{\varepsilon Nd}$ (t) values of + 9.52 and + 9.89. Sr is a mobile element during seawater alteration (Hart and Staudigel 1982), thus most of our samples were likely modified by seawater alteration.

Zircon U–Pb age and Hf isotopes

A total of 379 analyses of zircon grains from four sedimentary samples from the Kanguer mélange (Figs. 3, 6, 7) yielded 304 concordant ages (concordance % > 90% or < 110%). All the U–Pb and Lu–Hf isotopic data are shown in Appendix Tables 3 and 4, respectively. Only concordant ages are described and discussed below.

Zircons from sample 08K01 are 100 µm long, have length/width ratios of 1.3–2.0, prominent zones in CL images, and they have variable contents of Th (28–1623 ppm) and U (69–5065 ppm), and Th/U values of 0.12–1.35. Of one hundred and sixty analyzed zircon grains, one hundred and ten yielded concordant ages with major concordant age peaks at 288.1 ± 0. 56 Ma (60.4% of the total), a secondary peak at 433.3 ± 0. 97 Ma (32.4% of the total), and scattered ages at 1209.2 ± 5.8 Ma (7.2% of the total) (Fig. 11a). The youngest three zircon ages are 209 ± 16 Ma, 228 ± 5 Ma, and 236 ± 2 Ma, which give a mean age of 234 ± 14 Ma (Fig. 11b). This mean age is interpreted as the MDA of the sandstone. Lu–Hf isotopic analyses of the detrital zircons yielded $\varepsilon_{Hf}(t)$ values ranging from − 8.1 to + 13.2 (Fig. 12a).

Zircons from sample 08K02 are dark, irregular, have a grain-size of 120 µm, and clear zones in CL images. The zircons contain variable contents of Th (54–659 ppm) and U (59–2102 ppm), and Th/U values of 0.23–1.28. Of sixty analyzed zircon grains, fifty-nine yielded concordant ages with two major concordant age peaks at 288.32 ± 0. 55 Ma (47.5% of the total) and at 415.23 ± 0.82 Ma (45.8% of the total), and scattered ages at 879.1 ± 4.4 Ma (6.3% of the total) and 2361 ± 22 Ma (1.7% of the total) (Fig. 11c). The youngest three zircon ages are 241 ± 2 Ma, 243 ± 2 Ma, and 243 ± 3 Ma, which yield a mean age of 242.5 ± 1.3 Ma (Fig. 11d), which we interpret as the MDA of the sandstone. Lu–Hf isotopic analyses of the detrital zircons yield $\varepsilon_{Hf}(t)$ values ranging from − 12.6 to + 12.1 (Fig. 12a).

Zircons from sample 08K03 are irregular, are about 100 µm in size, and have sharp zones in CL images. The grains show variable contents of Th (24–1953 ppm) and U (44–3760 ppm), and Th/U values of 0.04–1.95. One hundred and sixty-one zircon grains were analyzed of which one hundred and thirty-five yield concordant ages with major and minor concordant age peaks at 292.18 ± 0. 52 Ma (64.9% of the total) and 436.9 ± 1.4 Ma (26.9% of the total), respectively (Fig. 11e). They also have scattered ages at 1001.6 ± 4.9 Ma (4.4% of the total) and 1510 ± 13 (3% of the total). The youngest three zircon ages are 236 ± 2 Ma, 237 ± 6 Ma, and 240 ± 5 Ma, which yield a mean age of 236.9 ± 2.0 Ma (Fig. 11f), which we interpret as the MDA of the sandstone. Lu–Hf isotopic analyses of the detrital zircons yield $\varepsilon_{Hf}(t)$ values ranging from − 16.5 to + 23.7 (Fig. 12a).

Discussion

Tectonic setting of the Kanguer mélange

The Kanguer mélange is characterized by block-in-matrix structures and has been thrust-imbricated. Blocks in the mélange consist of gabbro, massive basalt, pillow basalt, diabase dykes, chert, limestone, and sandstone, which are enclosed in a matrix of chlorite-phyllite schist and cleaved sandstone (Figs. 2, 3, 4, 5). On a kilometer scale, blocks of different lithologies are repeated several times and exhibit top-to-the-south imbricate structures (Figs. 2b, 6, 7). The sandstone blocks (Fig. 3a, d) and the matrix (Fig. 5) contain sub-vertical isoclinal folds, the axes of which strike

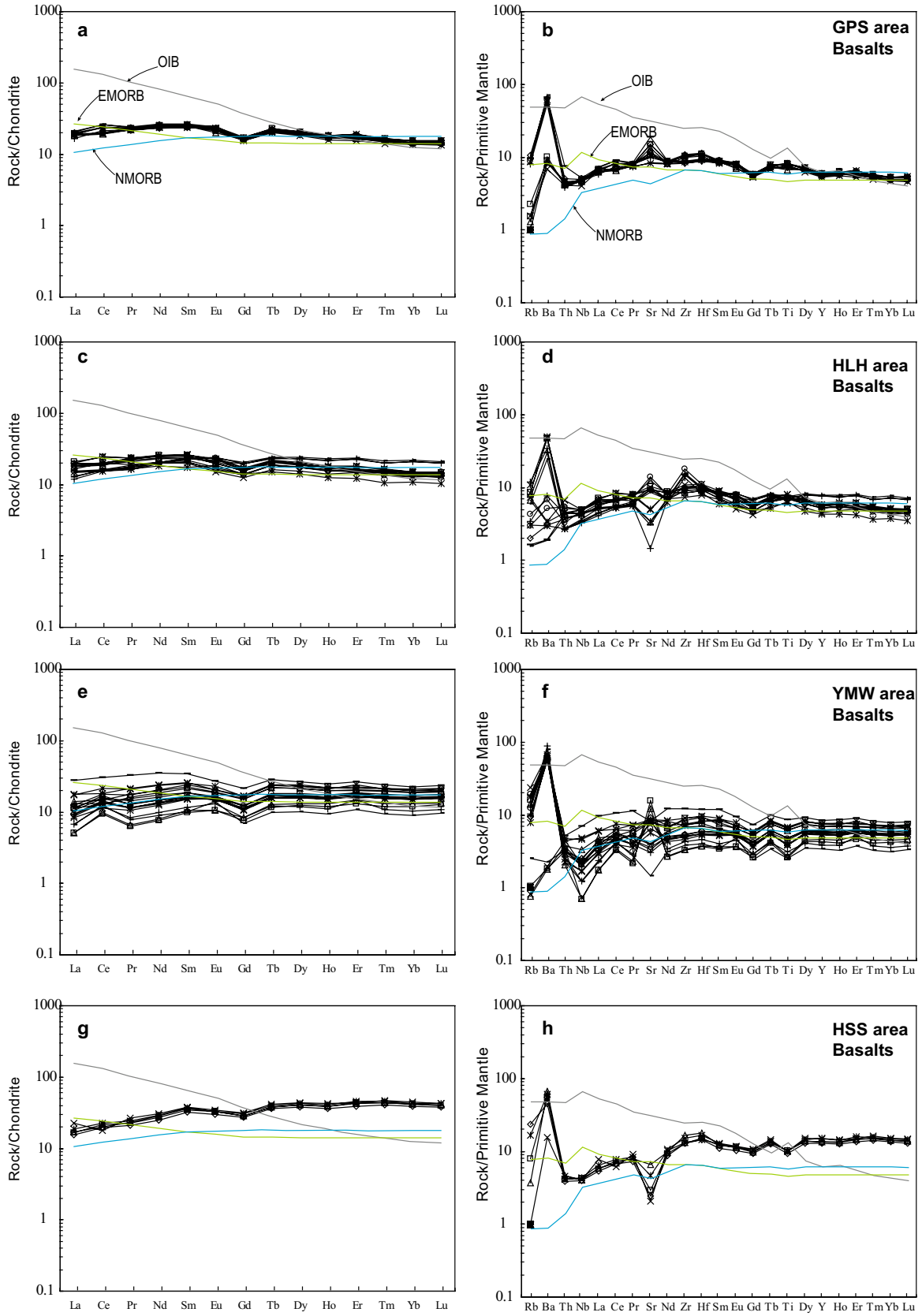
a
OIB
EMORB
NMORB
Rock/Chondrite
1000
100
10
1
0.1
La Ce Pr Nd Sm Eu Gd Tb Dy Ho Er Tm Yb Lu
b
GPS area
Basalts
OIB
EMORB
NMORB
Rock/Primitive Mantle
Rb Ba Th Nb La Ce Pr Sr Nd Zr Hf Sm Eu Gd Tb Ti Dy Y Ho Er Tm Yb Lu
c
d
HLH area
Basalts
e
f
YMW area
Basalts
g
h
HSS area
Basalts

◂**Fig. 9** Chondrite-normalized REE (**a**, **c**, **e**, and **f**) and Primitive Mantle (PM) normalized multi-element (**b**, **d**, **f**, and **g**) diagrams of basalts from the Kanguer mélange belt. Chondrite values are from (Boynton 1984). The PM values are from (Sun and McDonough 1989). All the blocks of basalt from the GPS, HLH, YMW, and HSS areas in the Kanguer mélange are similar to those of N-MORBs

east–west. All these structures indicate that the Kanguer mélange underwent intense top-to-the-south thrusting and shearing. The blocks of basalt, diabase, gabbro, limestone, and chert are probably fragments of oceanic plate stratigraphy, which, if intact, would have provided information on the travel history of the oceanic plate from ridge to trench (Kusky et al. 2013); the fragments are inter-mixed in the mélange and accreted into the accretionary complex (Festa et al. 2019; Raymond 2019; Wakabayashi 2019). Although no ultramafic blocks/serpentinized or otherwise crop out in the Kanguer mélange, some ophiolites were reported by Li et al. (2008) in the mélange to the northwest of our study area. Thus, the lithologies, field relationships, and structural characteristics indicate that the Kanguer mélange is a classic ophiolite-bearing tectonic mélange that formed at a convergent margin and was created by subduction-accretion processes (Kusky et al. 2020; Wakabayashi 2015; Xiao et al. 2015) (Fig. 8).

All the blocks of basalt from the GPS, HLH, YMW, and HSS areas in the Kanguer mélange are tholeiitic and have consistent geochemical compositions, suggesting they formed by the same petrogenetic processes. Their REE patterns (Fig. 9a, c, e, g) are similar to those of N-MORBs, as also are the similar trace element patterns with their positive Rb, Ba, and Sr anomalies (Fig. 9b, d, f, h). Their enrichments in fluid-soluble elements and ratios such as Sr–Nd isotopes indicate seawater alteration (Kelley et al. 2003) (Fig. 12b). In Th/Yb–Nb/Yb and V-Ti/1000 diagrams (Fig. 10c, d), most of the basalts plot in the field of N-MORB, but some in the island arc field, probably because of fluid enrichments due to seawater alteration (Furnes and Safonova 2019; Reagan et al. 2010). All the geochemical and Sr–Nd isotopic features demonstrate that the basalts in the Kanguer mélange belt were probably generated in a Mid-Ocean-Ridge, where erupted lavas were influenced by seawater penetration. We envisage that most of the basaltic blocks in the Kanguer mélange belt were scraped off a downgoing slab of oceanic crust, which had been generated in a Mid-Ocean-Ridge.

MDA of the Kanguer mélange

There are several methods for calculating the MDA of sedimentary rocks from their detrital zircon U–Pb ages (Coutts et al. 2019). Here we use the youngest three grains that overlap at a 2σ uncertainty. The sandstone samples (08K01, 08K02, and 08K03) yield mean ages of 234 ± 14 Ma, 242.5 ± 1.3 Ma, and 236.9 ± 2.0 Ma, respectively (Fig. 11b, d, f). All the youngest three grains overlap in age at a 2σ uncertainty, which indicates that the mean age for each sample is robust. The lag time between zircon crystallization and real deposition can be very short in some geologic settings, e.g., when a sediment is sourced from an active magmatic arc (Cawood et al. 2012). We interpret the MDA of each sample to indicate that the overall deposition was at 234 Ma in the late Middle Triassic (Ladinian).

The youngest MDA of the sandstone matrix of the Kanguer mélange belt was in the mid-Triassic, which indicates that the Kanguer Ocean still existed at 234 Ma, and that the final accretion of the Kanguer mélange was after the Ladinian.

Provenance of the Kanguer mélange

The Kanguer mélange is located between the intra-oceanic Dannanhu arc in the north and the Yamansu-CTS arc in the south (Fig. 1b). Therefore, these intra-oceanic island arcs were the main potential provenance for the sandstone matrix of the Kanguer mélange.

In the cross-sections of Fig. 6a and b the three sandstones (08K01, 02 and 03) have similar and consistent detrital zircon U–Pb age populations (Fig. 11a, c, e) with dominant age peaks in the period 288–292 Ma, a second peak at 415–436 Ma, and some scattered Precambrian ages (less than 8% of the total concordant ages for each sample). Lu–Hf isotopic analyses of these detrital zircons yielded $\varepsilon_{Hf}(t)$ values from − 16.5 to + 23.7 (Fig. 12a). The Dannanhu intra-oceanic arc contains major Permian and Ordovician magmatic rocks (but no Precambrian rocks), which are largely tholeiitic basalts and calc-alkaline andesites and granitoids that have subduction-related geochemical features with positive whole-rock $\varepsilon_{Nd}(t)$ and zircon $\varepsilon_{Hf}(t)$ values (Du et al. 2018a; Mao et al. 2019; Mao et al. 2014b; Qin et al. 2011; Wang et al. 2018; Yuan et al. 2010). The Dananhu arc is interpreted as an intra-oceanic arc that formed in the early Ordovician (Du et al. 2019; Xiao et al. 2004). Both the detrital zircon age spectra and $\varepsilon_{Hf}(t)$ values are comparable with the magmatic record in the Dananhu intra-oceanic arc. The sedimentary samples (08K01, 02, and 03) were probably derived from the Dananhu intra-oceanic arc in the north, which means that Kanguer mélange probably formed in the forearc of the Dananhu intra-oceanic arc.

Provenance variations in the Kanguer mélange

As discussed above, the Kanguer mélange is an accretionary complex, which indicates that the matrix of the mélange was scraped off from sediments of the downgoing slab. So,

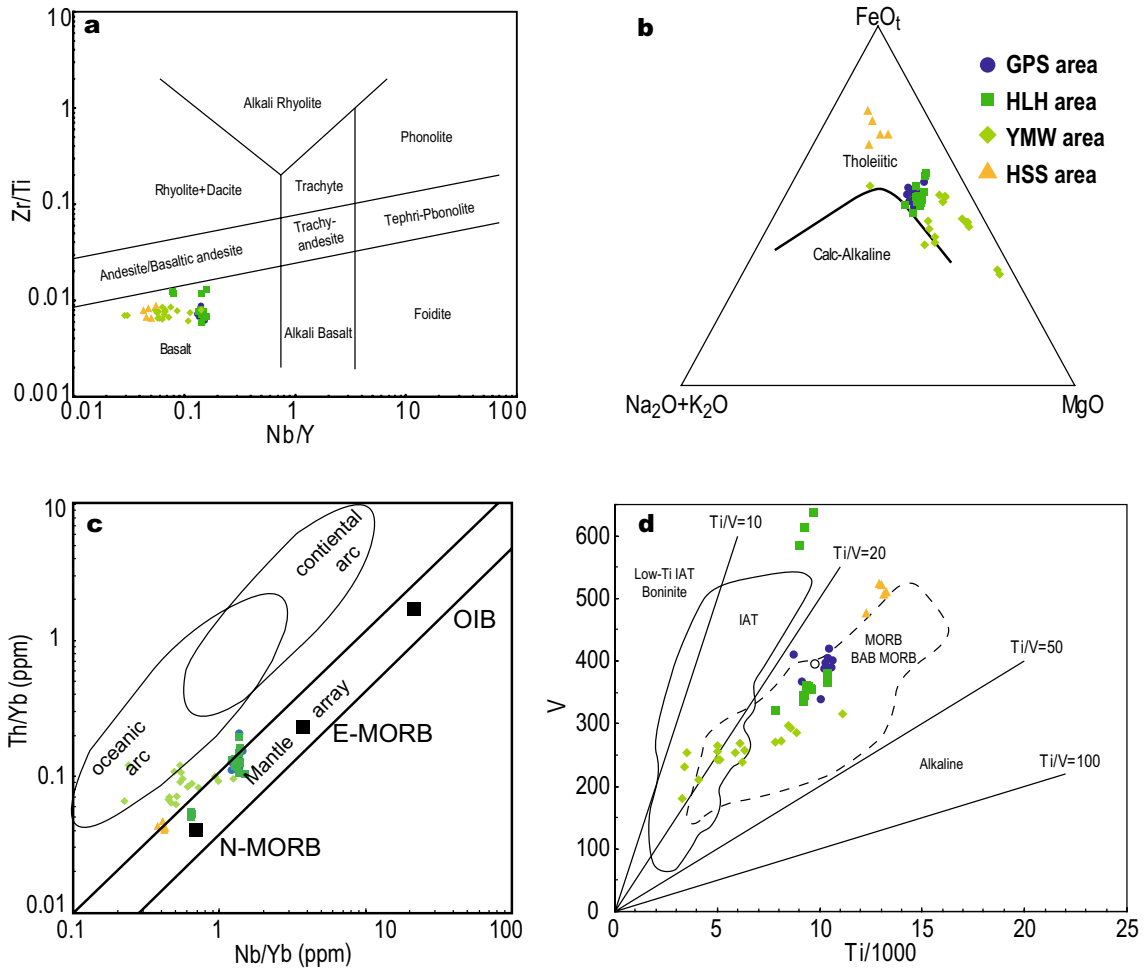

Fig. 10 Diagrams used for discrimination of tectonic settings of basalts from the Kanguer mélange belt. **a** The Zr/Ti vs. Nb/Y diagram after (Floyd et al. 1998), **b** AFM diagram after (Irvine and Baragar 1971), **c** Th/Yb vs. Nb/Yb after (Pearce 2008) and **d** V vs. Ti/1000 diagrams after (Shervais 1982). These diagrams demonstrate that the basalts in the Kanguer mélange belt were probably generated in a Mid-Ocean-Ridge

the provenance variations of the matrix can shed light on the spatiotemporal framework of the arc and accretionary complex.

The Kanguer Ocean subducted to the north and generated the Kanguer ophiolite (494 Ma) in a supra-subduction zone in the Late Cambrian (Li et al. 2008) and the Dananhu intra-oceanic arc in the Ordovician (Xiao et al. 2004). Therefore, the Kanguer mélange probably formed as early as the Ordovician. Chen et al. (2019) reported detrital zircon U–Pb age spectra in late Devonian sedimentary rocks in the Dananhu arc which have a unique age peak at ~ 400 Ma with no Precambrian ages (Chen et al. 2020), which suggests that the Kanguer Ocean between the Dananhu intra-oceanic arc and the Yamansu-CTS composite continental arc was quite wide in the Devonian. Our Triassic samples (08K01, 02, and 03) from the Kanguer mélange received sediments mainly from the Dananhu intra-oceanic arc in the north and very few from the Yamansu-CTS composite arc in the south, suggesting that the Kanguer Ocean was sufficiently narrow for their proximity. This provenance variation supports the idea that the Kanguer mélange formed in the forearc of the Dananhu intra-oceanic arc.

Tectonic evolution and implications for the Altaids

The Kanguer mélange belt has been interpreted as: (1) an inter-arc basin between the Dannanhu and Yamansu arcs (Han and Zhao 2018; Xiao et al. 2004); (2) a mélange in the terminal suture zone between the approaching Siberian craton and Tarim craton (Ma et al. 1997); (3) a short-lived limited ocean rifted on the accretionary wedge (Wang et al. 2019). The third interpretation is inappropriate, because, if the rifting was caused by an upwelling mantle plume, the basalts in the Kanguer mélange should display an oceanic island basalt (OIB) affinity, and the contact between basalts and their wall-rocks should be intrusive. However, all the

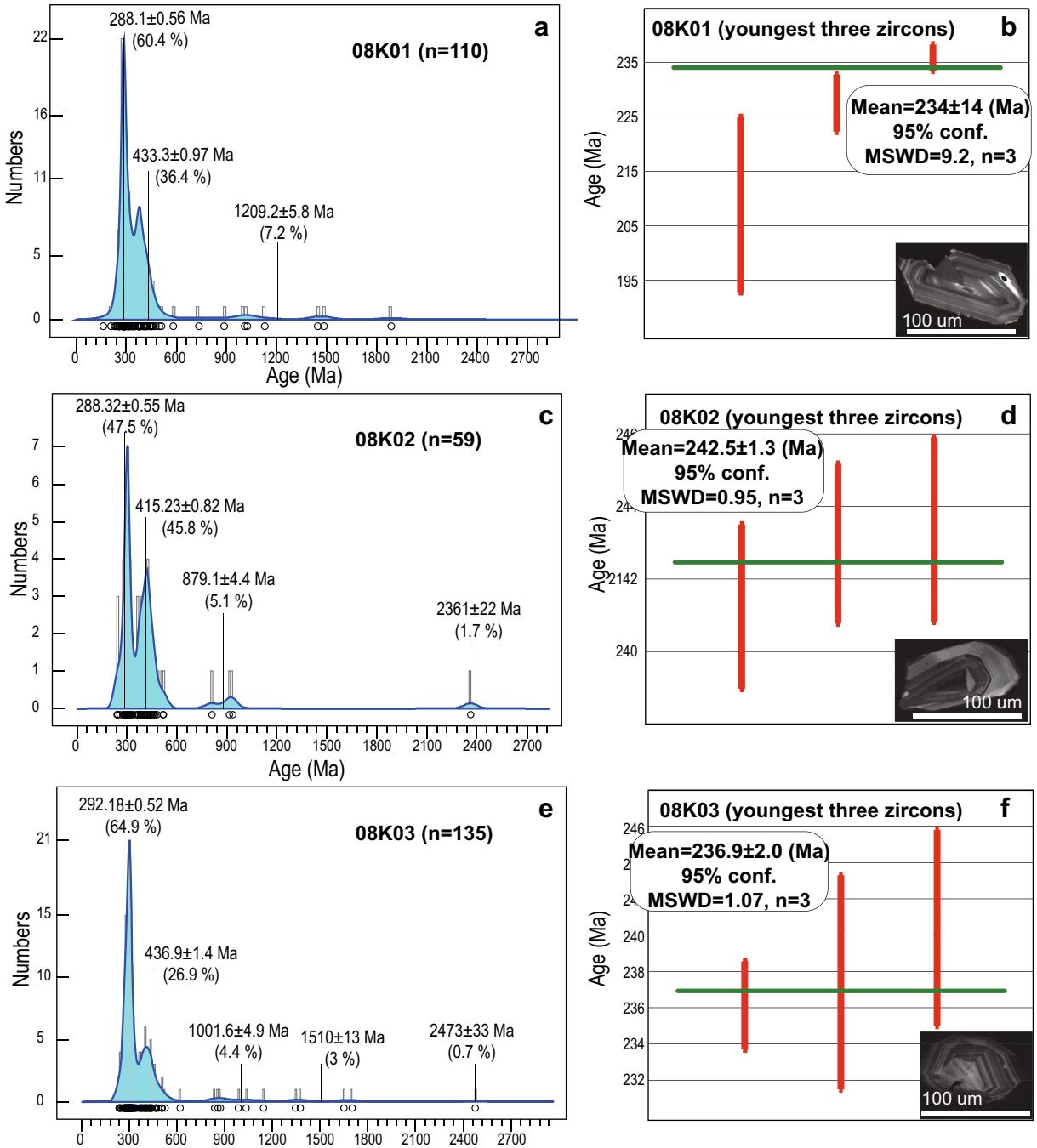

Fig. 11 **a**, **c**, **e**, **g** Histograms and normalized kernel density plots of the ages of detrital zircons in four sandstones in the HLH area from the Kanguer mélange (see Fig. 3 for sample locations and supporting information and Appendix Table 3 for data sources). Ages of $^{206}Pb/^{238}U$ and 1σ, which concordance % > 90% or < 110% are used to density plots by DensityPlotter software Version 8.5 (Vermeesch 2012). **b**, **d**, **f**, **h** MDAs for each sample. The MDA of each sample to indicate that the overall deposition was at 234 Ma in the late Middle Triassic (Ladinian), which indicates that the Kanguer Ocean still existed at 234 Ma. The youngest three ages of $^{206}Pb/^{238}U$ and 1σ, which concordance % > 90% or < 110% for each sample are used to calculate the mean age by Isoplot/Ex 2.2 (Ludwig 2001)

basalts in this study have an N-MORB signature and have been thrust within mélange matrix. The Kanguer ophiolite was reported to have formed in a supra-subduction zone at 494 Ma (SHRIMP zircon U–Pb age) (Li et al. 2008), which suggests that the Kanguer Ocean was open and being subducted in the late Cambrian. Therefore, the Kanguer Ocean was a long-lived branch of the Paleo-Asian Ocean in the southern Altaids.

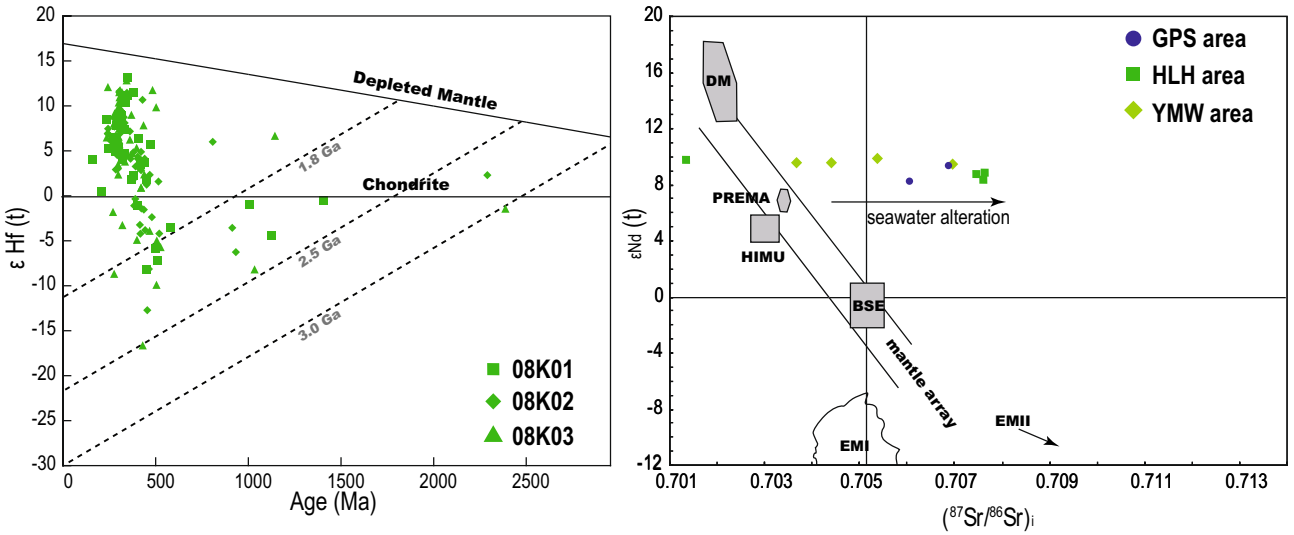

Fig. 12 **a** Hf isotopic diagram of dated sandstones from the Kanguer mélange showing that the sandstone samples (08K01, 02, and 03) were probably derived from the Dananhu intra-oceanic arc in the north. **b** $\varepsilon_{Nd}(t)$ vs. $(^{87}Sr/^{86}Sr)_i$ diagram of basalts from the Kanguer mélange, showing that the basalts were probably generated in a Mid-Ocean-Ridge, where erupted lavas were influenced by seawater penetration. All initial $^{87}Sr/^{86}Sr$ values are calculated to $t = 290$ Ma

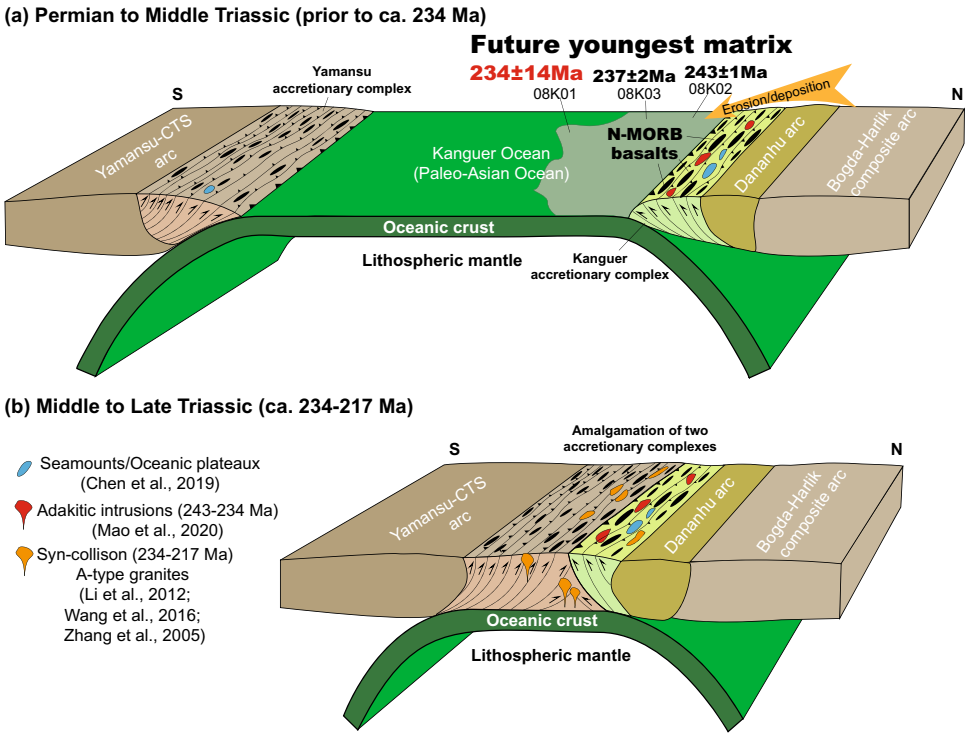

Fig. 13 Tectonic model showing two stages of evolution in the Eastern Tianshan. **a** In the Permian to Middle Triassic, the Kanguer ocean, a branch of the Paleo-Asian Ocean, remained open and was subducting on both sides. The blocks of N-MORB-affinity, diabase, limestone, and chert were accreted to the fore-arc of the Dananhu arc of the growing Kanguer accretionary complex, in which detrital zircons in the youngest matrix sediments have MDAs of 234 Ma. **b** In the Middle to Late Triassic (234–217 Ma), the Kanguer ocean closed by double subduction, and the Dananhu intra-oceanic island arc was amalgamated with the Yamansu-CTS continental arc. Large syn- to post-collisional granodiorite plutons intruded the two arcs and their accretionary complexes

The final closure time of the Paleo-Asian Ocean is controversial: 1. late Carboniferous (Han and Zhao 2018; Wang et al. 2016; Wu et al. 2016; Zhang et al. 2005); 2. late Permian to early Triassic (Chen et al. 2019; Huang et al. 2018; Mao et al. 2020; Mao et al. 2014a; Xiao et al. 2018; Zhang et al. 2007; Zheng et al. 2020). The late Carboniferous time of final closure of the Paleo-Asian Ocean in the Eastern Tianshan is mainly based on the following evidence: (1) No ophiolites or ultrahigh-pressure metamorphic rocks younger than 300 Ma have been found in the eastern North Tianshan suture (Han and Zhao 2018). (2) an $^{40}Ar/^{39}Ar$ age of 278–254 Ma on biotite and hornblende from granitic plutons reflects collision-induced regional metamorphism and deformation (Wang et al. 2008). However, this evidence is

circumstantial and not robust. First, the formation age of an ophiolite only indicates the time when oceanic crust was generated and does not provide information on the time of ophiolite emplacement and the ocean closure (Coleman 1981; Dilek and Furnes 2011). Second, the $^{40}Ar/^{39}Ar$ age of biotite and hornblende can also be interpreted as the time of a magmatic reset of the Ar–Ar system, particularly in view of the fact that ca. 275–267 Ma mafic-intermediate intrusions occur in the same area (zircon U–Pb ages, (Wang et al. 2014)). Moreover, juvenile magmatic arc accretion and continental growth are characteristic of the Altaids, which was commonly produced by oceanic slab subduction and intrusion in accretionary prisms (Jahn 2004; Jahn et al. 2000; Windley et al. 2007; Xiao et al. 2015). Therefore, only the age of the youngest subduction-related intrusions can be used to define the final amalgamation age in a long-lived accretionary orogenic belt such as the Altaids.

Accordingly, we update our tectonic model of the Eastern Tianshan in the southern Altaids (Fig. 13) using our new and published data in the light of the above discusssion. Our new detrital zircon U–Pb ages of matrix sandstones indicate that one major branch of the Paleo-Asian Ocean, the Kanguer ocean, was still open at ca. 234 Ma. The youngest 234 Ma age of the matrix in the Kanguer accretionary mélange that contains blocks of N-MORB basalts provides a snapshot of the mid-Triassic northward subduction of the Paleo-Asian Ocean in the Eastern Tianshan (Fig. 13a). This tectonic scenario is consistent with the presence of 243–234 Ma adakites, which were generated by slab-melted, lower crust of the Dananhu arc (Mao et al. 2020). In the Middle to Late Triassic (234–217 Ma), the Kanguer ocean closed, and the Dananhu intra-oceanic arc was amalgamated and welded with the Yamansu-CTS continental arc (Fig. 13b). Large-scale syn- to post-collisional granites intruded in the Eastern Tianshan in the Late Triassic (Li et al. 2012; Wang et al. 2016).

Combined with the Mid-Late Triassic peak metamorphic ages of eclogites in the Western Tianshan (Sang et al. 2017, 2020; Zhang et al. 2007), we consider that the final time of amalgamation of the southern Altaids, recorded in the whole Tianshan orogenic belt, was most likely in the Late Triassic.

Conclusions

(1) Field relations and map data indicate that the Kanguer mélange has a characteristic block-in-matrix structure and it underwent intense top-to-the-south thrusting and shearing. The blocks of basalt, diabase, gabbro, limestone, and chert are probably fragments derived from a downgoing oceanic plate, which were accreted to the evolving accretionary complex.

(2) Geochemical and isotopic data of basalts from the Kanguer mélange belt have the same diagnostic signatures as those of N-MORBs.

(3) The MDAs of sandstones from the matrix of the Kanguer mélange belt are 234 ± 14 Ma, 242.5 ± 1.3 Ma, 236.9 ± 2.0 Ma and 274 ± 3 Ma, which indicates that the Kanguer Ocean was still open at 234 Ma.

(4) The basalts and sandstone occur in imbricate thrust slices, suggesting the accretion of the Kanguer mélange belt should be later than 234 Ma. The final time of amalgamation of the southern Altaids in the whole Tianshan orogenic belt was probably in the mid-late Triassic.

Appendix analytical methods

Zircon U–Pb analyses were performed at the Beijing Quick-Thermo Science & Technology Co., Ltd, using an ESI New Wave NWR 193UC (TwoVol2) laser ablation system connected to an Agilent 8900 ICP–QQQ, following analytical procedures described in (Ji et al. 2020). In situ zircon Lu–Hf isotopic were analyzed with a Neptune Multi-Collector ICP-MS equipped with a Geolas-193 laser-ablation system. Lu–Hf isotopic data were obtained from the same dated zircon grains (Wu et al. 2006).

The whole-rock trace elements were analyzed by Inductively Coupled Plasma Mass Spectrometry on an Agilent 7500a in the Institute of Geology and Geophysics, Chinese Academy of Sciences (IGGCAS) in Beijing. The detailed procedure followed that of Yang et al. (2012).

About 100 mg of whole-rock powder was decomposed in a mixture of HF–$HClO_4$ in Teflon beakers to which appropriate amounts of mixed ^{87}Rb–^{86}Sr and ^{149}Sm–^{150}Nd were added. The isotopic ratios were measured on a MAT262 IsoProbe-T thermal ionization mass spectrometer in the IGGCAS. The detailed analytical procedures for the chemical separation and isotopic measurements were described by Chu (2009).

Supplementary Information The online version contains supplementary material available at https://doi.org/10.1007/s00531-021-01990-5.

Acknowledgments We appreciate Prof. Albrecht von Quadt and two anonymous reviewers for their constructive and valuable comments, which substantially enhanced the final presentation of the paper. This study was financially supported by the National Natural Science Foundation of China (41822204, 41888101, 91855207), the National Key R & D Program of China (2017YFC0601206), the Key Research Program of Frontier Sciences of CAS (QYZDJ-SSW-SYS012), the Strategic Priority Research Program (B) of the Chinese Academy of Sciences (CAS) (XDB18020203), and CAS Project of the China-Pakistan Joint Research Center on Earth Sciences (131551KYSB20200021). This is a contribution to IGCP 662.

References

Ao SJ, Xiao WJ, Windley BF, Mao QG, Zhang JE, Zhang ZY (2020) Ordovician to Early Permian accretionary tectonics of Eastern Tianshan: insights from Kawabulak ophiolitic melange, granitoid, and granitic gneiss. Geol J 55:280–298. https://doi.org/10.1002/gj.3371

Bazhenov ML, Collins AQ, Degtyarev KE, Levashova NM, Mikolaichuk AV, Pavlov VE, Van der Voo R (2003) Paleozoic northward drift of the North Tien Shan (Central Asia) as revealed by Ordovician and Carboniferous paleomagnetism. Tectonophysics 366:113–141. https://doi.org/10.1016/S0040-1951(03)00075-1

Benyon C, Leier A, Leckie DA, Webb A, Hubbard SM, Gehrels G (2014) Provenance of the Cretaceous Athabasca Oil Sands, Canada: implications for continental-scale sediment transport. J Sediment Res 84:136–143. https://doi.org/10.2110/jsr.2014.16

Boynton WV (1984) Geochemistry of the rare earth elements: meteorite study. In: Henderson P (ed) Rare earth element geochemistry. Elsevier, Amsterdam, pp 63–114

Buchan C et al (2002) Timing of accretion and collisional deformation in the Central Asian orogenic belt: implications of granite geochronology in the Bayankhongor ophiolite zone. Chem Geol 192:23–45

Cardozo N, Allmendinger RW (2013) Spherical projections with OSX-Stereonet. Comput Geosci 51:193–205. https://doi.org/10.1016/j.cageo.2012.07.021

Cawood PA, Hawkesworth CJ, Dhuime B (2012) Detrital zircon record and tectonic setting. Geology 40:875–878. https://doi.org/10.1130/g32945.1

Chen Z et al (2019) Composition, Provenance, and Tectonic Setting of the Southern Kangurtag Accretionary Complex in the Eastern Tianshan, NW China: implications for the Late Paleozoic Evolution of the North Tianshan Ocean. Tectonics 38:2779–2802. https://doi.org/10.1029/2018tc005385

Chen Z et al (2020) Latest Permian–early Triassic arc amalgamation of the Eastern Tianshan (NW China): constraints from detrital zircons and Hf isotopes of Devonian-Triassic sediments. Geol J 55:1708–1727. https://doi.org/10.1002/gj.3540

Chu Z, Chen F, Yang Y, Guo J (2009) Precise determination of Sm, Nd concentrations and Nd isotopic compositions at the nanogram level in geological samples by thermal ionization mass spectrometry. J Anal At Spectrom 24:1534–1544. https://doi.org/10.1039/B904047A

Coleman RG (1981) Tectonic setting for ophiolite obduction in Oman. J Geophys Res 86:2497–2508. https://doi.org/10.1029/JB086iB04p02497

Coleman RG (1989) Continental growth of Northwest China. Tectonics 8:521–635

Coutts DS, Matthews WA, Hubbard SM (2019) Assessment of widely used methods to derive depositional ages from detrital zircon populations. Geosci Front 10:1421–1435. https://doi.org/10.1016/j.gsf.2018.11.002

Dilek Y, Furnes H (2011) Ophiolite genesis and global tectonics: geochemical and tectonic fingerprinting of ancient oceanic lithosphere. Geol Soc Am Bull 123:387–411. https://doi.org/10.1130/b30446.1

Dobretsov NL, Berzin NA, Buslov MM (1995) Opening and the tectonic evolution of Paleo-Asian ocean. Int Geol Rev 35:335–360

Du L, Long X, Yuan C, Zhang Y, Huang Z, Sun M, Xiao W (2018a) Petrogenesis of Late Paleozoic diorites and A-type granites in the central Eastern Tianshan, NW China, Response to post-collisional extension triggered by slab breakoff. Lithos 318–319:47–59. https://doi.org/10.1016/j.lithos.2018.08.006

Du L, Long X, Yuan C, Zhang Y, Huang Z, Wang X, Yang Y (2018b) Mantle contribution and tectonic transition in the Aqishan-Yamansu Belt, Eastern Tianshan, NW China: Insights from geochronology and geochemistry of Early Carboniferous to Early Permian felsic intrusions. Lithos 304–307:230–244. https://doi.org/10.1016/j.lithos.2018.02.010

Du L, Zhang Y, Huang Z, Li X-P, Yuan C, Wu B, Long X (2019) Devonian to carboniferous tectonic evolution of the Kangguer Ocean in the Eastern Tianshan NW China: Insights from three episodes of granitoids. Lithos 350–351:105243. https://doi.org/10.1016/j.lithos.2019.105243

Fedo CM, Sircombe KN, Rainbird RH (2003) Detrital zircon analysis of the sedimentary record. In: Hanchar JM, Hoskin PWO (eds) Zircon, vol 53. Reviews in Mineralogy & Geochemistry, pp 277–303. doi:https://doi.org/10.2113/0530277

Festa A, Pini GA, Ogata K, Dilek Y (2019) Diagnostic features and field-criteria in recognition of tectonic, sedimentary and diapiric mélanges in orogenic belts and exhumed subduction-accretion complexes. Gondwana Res 74:7–30. https://doi.org/10.1016/j.gr.2019.01.003

Floyd PA, Yaliniz MK, Goncuoglu MC (1998) Geochemistry and petrogenesis of intrusive and extrusive ophiolitic plagiogranites, Central Anatolian Crystalline Complex, Turkey. Lithos 42:225–241. https://doi.org/10.1016/s0024-4937(97)00044-3

Furnes H, Safonova I (2019) Ophiolites of the Central Asian Orogenic Belt: Geochemical and petrological characterization and tectonic settings. Geosci Front 10:1255–1284. https://doi.org/10.1016/j.gsf.2018.12.007

Gao J, Klemd R (2003) Formation of HP-LT rocks and their tectonic implications in the western Tianshan Orogen, NW China: geochemical and age constraints. Lithos 66:1–22. https://doi.org/10.1016/s0024-4937(02)00153-6

Han Y, Zhao G (2018) Final amalgamation of the Tianshan and Junggar orogenic collage in the southwestern Central Asian Orogenic Belt: constraints on the closure of the Paleo-Asian Ocean. Earth Sci Rev 186:129–152. https://doi.org/10.1016/j.earscirev.2017.09.012

Hart SR, Staudigel H (1982) The control of alkalies and uranium in seawater by ocean crust alteration. Earth Planet Sci Lett 58:202–212. https://doi.org/10.1016/0012-821X(82)90194-7

Huang B, Fu D, Kusky T, Ruan K, Zhou W, Zhang X (2018) Sedimentary provenance in response to Carboniferous arc-basin evolution of East Junggar and North Tianshan belts in the southwestern Central Asian Orogenic Belt. Tectonophysics 722:324–341. https://doi.org/10.1016/j.tecto.2017.11.015

Irvine TN, Baragar WRA (1971) A guide to the chemical classification of the common volcanic rocks. Can J Earth Sci 8:523–548. https://doi.org/10.1139/e71-055

Jahn BM (2004) The Central Asian Orogenic Belt and growth of the continental crust in the Phanerozoic. Geol Soc Lond 226:73–100

Jahn BM, Wu FY, Chen B (2000) Massive granitoid generation in Central Asia: Nd isotope evidence and implication for continental growth in the Phanerozoic. Episodes 23:82–92

Ji W-Q et al (2020) Early Evolution of Himalayan Orogenic Belt and Generation of Middle Eocene Magmatism: constraint From Haweng Granodiorite Porphyry in the Tethyan Himalaya. Front Earth Sci. https://doi.org/10.3389/feart.2020.00236

Kelley KA, Plank T, Ludden J, Staudigel H (2003) Composition of altered oceanic crust at ODP Sites 801 and 1149 Geochemistry. Geophys Geosyst. https://doi.org/10.1029/2002gc000435

Kusky TM, Windley BF, Safonova I, Wakita K, Wakabayashi J, Polat A, Santosh M (2013) Recognition of ocean plate stratigraphy in accretionary orogens through Earth history: a record of 3.8 billion years of sea floor spreading, subduction, and accretion Gondwana. Research 24:501–547. https://doi.org/10.1016/j.gr.2013.01.004

Kusky T et al (2020) Mélanges through time: life cycle of the world's largest Archean mélange compared with Mesozoic and Paleozoic subduction-accretion-collision mélanges. Earth Sci Rev. https://doi.org/10.1016/j.earscirev.2020.103303

Li WQ, Ma H, Wang R, Xia B (2008) SHRIMP dating and Nd-Sr isotopic Tracing of Kangguertage ophiolite in eastern Tianshan, Xinjiang. Acta Petrol Sin 24:773–780 ((**in Chinese with English abstract**))

Li S, Wang T, Wilde SA, Tong Y, Hong D, Guo Q (2012) Geochronology, petrogenesis and tectonic implications of Triassic granitoids from Beishan, NW China. Lithos 134–135:123–145

Long X, Wu B, Sun M, Yuan C, Xiao W, Zuo R (2020) Geochronology and geochemistry of Late Carboniferous dykes in the Aqishan-Yamansu belt, eastern Tianshan: evidence for a post-collisional slab breakoff. Geosci Front 11:347–362. https://doi.org/10.1016/j.gsf.2019.06.003

Ludwig KR (2001) Users manual for Isoplot/Ex rev. 2.49. Berkeley Geochronology Centre Special Publication. No. 1a, 56 pp

Luo T, Liao Q-A, Zhang X-H, Chen J-P, Wang G-C, Huang X (2016) Geochronology and geochemistry of Carboniferous metabasalts in eastern Tianshan Central Asia: evidence of a back-arc basin. Int Geol Rev 58:756–772. https://doi.org/10.1080/00206814.2015.1114433

Ma RS, Shu LS, Sun J (1997) Tectonic evolution and metallogeny of Eastern Tianshan mountains. Geological Publishing House, Beijing

Ma X, Shu L, Meert JG, Li J (2014) The Paleozoic evolution of Central Tianshan: geochemical and geochronological evidence. Gondwana Res 25:797–819. https://doi.org/10.1016/j.gr.2013.05.015

Mao QG et al. (2014b) Geochronology, geochemistry and petrogenesis of Early Permian alkaline magmatism in the Eastern Tianshan: Implications for tectonics of the Southern Altaids. Lithos 190–191:37–51

Mao QG, Wang JB, Xiao WJ, Fang TH, Yu MJ, Ao SJ, Zhang JE (2014) Stratigraphic, U-Pb (Zircon) and geochemical constraints on magmas, mineralization and geological evolution of the Kalatage destrict, the central part of Dananhu arc in eastern Tianshan Mountains. Acta Geol Sin 88:885–886

Mao Q et al (2018) Skarn-mineralized porphyry adakites in the Harlik arc at Kalatage, E. Tianshan (NW China): Slab melting in the Devonian-early Carboniferous in the southern Central Asian Orogenic Belt. J Asian Earth Sci 153:365–378. https://doi.org/10.1016/j.jseaes.2017.03.021

Mao QG et al (2019) Mineralization of an intra-oceanic arc in an accretionary orogen: Insights from the early Silurian Honghai VMS Cu-Zn deposit and associated adakites of the Eastern Tianshan (NW China). Geol Soc Am Bull 131:803–830

Mao QG, Ao SJ, Windley BF, Wang JB, Li YC, Xiao WJ (2020) Middle Triassic lower crust-derived adakitic magmatism: thickening of the Dananhu intra-oceanic arc and its implications for arc-arc amalgamation in the Eastern Tianshan (NW China). J Geol Soc In press

Matthews WA, Guest B, Coutts D, Bain H, Hubbard S (2017) Detrital zircons from the Nanaimo basin, Vancouver Island, British Columbia: an independent test of Late Cretaceous to Cenozoic northward translation. Tectonics 36:854–876. https://doi.org/10.1002/2017tc004531

Nelson DR (2001) An assessment of the determination of depositional ages for precambrian clastic sedimentary rocks by U-Pb dating of detrital zircons. Sed Geol 141–142:37–60. https://doi.org/10.1016/S0037-0738(01)00067-7

Pearce JA (2008) Geochemical fingerprinting of oceanic basalts with applications to ophiolite classification and the search for Archean oceanic crust. Lithos 100:14–48. https://doi.org/10.1016/j.lithos.2007.06.016

Qin KZ et al (2011) SIMS zircon U-Pb geochronology and Sr-Nd isotopes of Ni-Cu-bering mafic-ultramafid intrusions in easterm Tianshan and Beishan in correrlation with flood basalts in Tarim basin (NW China): constraints on a CA 280Ma mantle plume. Am J Sci 311:237–260

Raymond LA (2019) Perspectives on the roles of melanges in subduction accretionary complexes: a review. Gondwana Res 74:68–89. https://doi.org/10.1016/j.gr.2019.03.005

Reagan MK et al (2010) Fore-arc basalts and subduction initiation in the Izu-Bonin-Mariana system Geochemistry. Geophys Geosyst. https://doi.org/10.1029/2009gc002871

Sang M, Xiao W, Bakirov A, Orozbaev R, Sakiev K, Zhou K (2017) Oblique wedge extrusion of UHP/HP complexes in the Late Triassic: structural analysis and zircon ages of the Atbashi Complex South Tianshan, Kyrgyzstan. Int Geol Rev 59:1369–1389. https://doi.org/10.1080/00206814.2016.1241163

Sang M, Xiao W, Windley BF (2020) Unravelling a Devonian-Triassic seamount chain in the South Tianshan high-pressure/ultrahigh-pressure accretionary complex in the Atbashi area (Kyrgyzstan). Geol J 55:2300–2317. https://doi.org/10.1002/gj.3776

Şengör AMC, Natal'in B (1996) Turkic-type orogeny and its role in the making of the continental crust. Ann Rev Earth Planet Sci 24:263–337

Şengör AMC, Natal'in BA, Burtman US (1993) Evolution of the Altaid tectonic collage and Paleozoic crustal growth in Eurasia. Nature 364:209–304

Sharman GR, Graham SA, Grove M, Kimbrough DL, Wright JE (2015) Detrital zircon provenance of the Late Cretaceous-Eocene California forearc: influence of Laramide low-angle subduction on sediment dispersal and paleogeography. Geol Soc Am Bull 127:38–60. https://doi.org/10.1130/b31065.1

Shervais JW (1982) Ti-V plots and the petrogenesis of modern and ophiolitic lavas. Earth Planet Sci Lett 59:101–118

Sickmann ZT, Schwartz TM, Graham SA (2018) Refining stratigraphy and tectonic history using detrital zircon maximum depositional age: an example from the Cerro Fortaleza Formation Austral Basin, southern Patagonia Basin. Research 30:708–729. https://doi.org/10.1111/bre.12272

Sun SS, McDonough WF (1989) Chemical and isotopic systematic of oceanic basalts: implicattions for mantle composition and process. In: Sauders AD, Norry MJ (eds) Magmatism in the Ocean Basins. Geological Society special Publication, 42, pp 3l3–345

Vermeesch P (2012) On the visualisation of detrital age distributions. Chem Geol 312–313:190–194. https://doi.org/10.1016/j.chemgeo.2012.04.021

Wakabayashi J (2015) Anatomy of a subduction complex: architecture of the Franciscan Complex, California, at multiple length and time scales. Int Geol Rev 57:669–746. https://doi.org/10.1080/00206814.2014.998728

Wakabayashi J (2019) Sedimentary compared to tectonically-deformed serpentinites and tectonic serpentinite mélanges at outcrop to petrographic scales: unambiguous and disputed examples from California. Gondwana Res 74:51–67. https://doi.org/10.1016/j.gr.2019.04.005

Wang Y, Li J, Sun G (2008) Postcollisional Eastward extrusion and tectonic exhumation along the Eastern Tianshan Orogen, Central Asia: constraints from dextral strike-slip motion and 40Ar/39Ar geochronological evidence. J Geol 116:599–618. https://doi.org/10.1086/591993

Wang B et al (2014) Late Paleozoic pre- and syn-kinematic plutons of the Kangguer-Huangshan Shear zone: Inference on the tectonic evolution of the eastern Chinese north Tianshan. Am J Sci 314:43–79. https://doi.org/10.2475/01.2014.02

Wang YH, Xue CJ, Liu JJ, Zhang FF (2016) Geological, geochronological, geochemical, and Sr-Nd-O-Hf isotopic constraints on origins of intrusions associated with the Baishan porphyry Mo deposit in eastern Tianshan, NW China. Miner Depos 51:953–969

Wang Y et al (2018) Paleozoic tectonic evolution of the Dananhu-Tousuquan island arc belt, Eastern Tianshan: Constraints from the magmatism of the Yuhai porphyry Cu deposit, Xinjiang, NW

China. J Asian Earth Sci 153:282–306. https://doi.org/10.1016/j.jseaes.2017.05.022

Wang GC et al (2019) New understanding of the tectonic framework and evolution during the Neoproterozoic-Paleozoic era in the East Tianshan mountains. J Geomech 25:798–819

Wilhem C, Windley BF, Stampfli GM (2012) The Altaids of Central Asia: a tectonic and evolutionary innovative review. Earth Sci Rev 113:303–341

Windley BF, Allen MB, Zhang C, Zhao ZY, Wang GR (1990) Paleozoic accretion and Cenozoic redeformation of the Chinese Tien Shan Range Central Asia. Geology 18:128–131

Windley BF, Alexeiev D, Xiao W, Kröner A, Badarch G (2007) Tectonic models for accretion of the Central Asian Orogenic belt. J Geol Soc Lond 164:31–47

Wu FY, Yang YH, Xie LW, Yang JH, Xu P (2006) Hf isotopic compositions of the standard zircons and baddeleyites used in U-Pb geochronology. Chem Geol 234:105–126. https://doi.org/10.1016/j.chemgeo.2006.05.003

Wu YS, Zhou KF, Li N, Chen YJ (2016) Zircon U-Pb dating and Sr–Nd–Pb–Hf isotopes of the ore-associated porphyry at the giant Donggebi Mo deposit Eastern Tianshan, NW China. Ore Geol Rev 2:794–807

XBGMR (1993) Regional Geology of Xinjiang Autonomous Region, Geological Memoirs, Ser. 1, No. 32, Map Scale 1: 1,500,000. Geological Publishing House, Beijing

Xiao WJ, Zhang LC, Qin KZ, Sun S, Li JL (2004) Paleozoic accretionary and collisional tectonics of the Eastern Tianshan (China): implications for the continental growth of central Asia. Am J Sci 304:370–395

Xiao WJ et al (2010) Paleozoic multiple accretionary and collisional processes of the Beishan orogenic collage. Am J Sci 310:1553–1594

Xiao W, Windley BF, Allen MB, Han C (2013) Paleozoic multiple accretionary and collisional tectonics of the Chinese Tianshan orogenic collage. Gondwana Res 23:1316–1341. https://doi.org/10.1016/j.gr.2012.01.012

Xiao WJ et al (2015) A tale of amalgamation of three permo-triassic collage systems in Central Asia: oroclines, sutures, and terminal accretion. Annu Rev Earth Pl Sc 43:477–507. https://doi.org/10.1146/annurev-earth-060614-105254

Xiao WJ et al (2018) Late Paleozoic to early Triassic multiple roll-back and oroclinal bending of the Mongolia collage in Central Asia. Earth Sci Rev 186:94–128

Yang J-H, Sun J-F, Zhang J-H, Wilde SA (2012) Petrogenesis of Late Triassic intrusive rocks in the northern Liaodong Peninsula related to decratonization of the North China Craton: Zircon U-Pb age and Hf–O isotope evidence. Lithos 153:108–128. https://doi.org/10.1016/j.lithos.2012.06.023

Yuan C, Sun M, Wilde S, Xiao WJ, Xu YG, Long XP, Zhao GC (2010) Postcollisional plutons in the Balikun area, East Chinese Tianshan: evolving magmatism in response to extension and slab break-off. Lithos 119:269–288

Zhang L, Xiao W, Qin K, Qu W, Du A (2005) Re–Os isotopic dating of molybdenite and pyrite in the Baishan Mo–Re deposit, eastern Tianshan NW China, and its geological significance. Mineral Depos 39:960–969

Zhang L et al (2007) Triassic collision of western Tianshan orogenic belt, China: evidence from SHRIMP U-Pb dating of zircon from HP/UHP eclogitic rocks. Lithos 96:266–280

Zheng R, Li J, Zhang J, Xiao W, Wang Q (2020) Permian oceanic slab subduction in the southmost of Central Asian Orogenic Belt: evidence from adakite and high-Mg diorite in the southern Beishan. Lithos. https://doi.org/10.1016/j.lithos.2020.105406

Zhou MF, Lesher CM, Yang ZX, Li JW, Sun M (2004) Geochemistry and petrogenesis of 270 Ma Ni-Cu-(PGE) sulfide-bearing mafic intrusions in the Huangshan district, Eastern Xinjiang, Northwest China: implications for the tectonic evolution of the Central Asian orogenic belt. Chem Geol 209:233–257